



Contents lists available at ScienceDirect

Engineering

journal homepage: www.elsevier.com/locate/eng

Article

Safe Motion Planning and Control Framework for Automated Vehicles with Zonotopic TRMPC

Hao Zheng^{a,b}, Yinong Li^{a,*}, Ling Zheng^a, Ehsan Hashemi^b

^aState Key Laboratory of Mechanical Transmissions, College of Mechanical and Vehicle Engineering, Chongqing University, Chongqing 400044, China

^bDepartment of Mechanical Engineering, University of Alberta, Edmonton, AB T6G 2H5, Canada

ARTICLE INFO

Article history:

Available online xxxx

Keywords:

Automated vehicles
Automated driving
Motion planning
Motion control
Tube MPC
Zonotope

ABSTRACT

Model mismatches can cause multi-dimensional uncertainties for the receding horizon control strategies of automated vehicles (AVs). The uncertainties may lead to potentially hazardous behaviors when the AV tracks ideal trajectories that are individually optimized by the AV's planning layer. To address this issue, this study proposes a safe motion planning and control (SMPAC) framework for AVs. For the control layer, a dynamic model including multi-dimensional uncertainties is established. A zonotopic tube-based robust model predictive control scheme is proposed to constrain the uncertain system in a bounded minimum robust positive invariant set. A flexible tube with varying cross-sections is constructed to reduce the controller conservatism. For the planning layer, a concept of safety sets, representing the geometric boundaries of the ego vehicle and obstacles under uncertainties, is proposed. The safety sets provide the basis for the subsequent evaluation and ranking of the generated trajectories. An efficient collision avoidance algorithm decides the desired trajectory through the intersection detection of the safety sets between the ego vehicle and obstacles. A numerical simulation and hardware-in-the-loop experiment validate the effectiveness and real-time performance of the SMPAC. The result of two driving scenarios indicates that the SMPAC can guarantee the safety of automated driving under multi-dimensional uncertainties.

© 2024 THE AUTHORS. Published by Elsevier LTD on behalf of Chinese Academy of Engineering and Higher Education Press Limited Company. This is an open access article under the CC BY-NC-ND license (<http://creativecommons.org/licenses/by-nc-nd/4.0/>).

1. Introduction

1.1. Motivation

Automated vehicles (AVs) have become a critical link in the development of intelligent transportation systems (ITS) owing to their vast potential to enhance safety, reduce energy consumption, and optimize traffic flow [1,2]. The general hierarchical scheme of an AV consists of three layers: ① perception layer, ② planning layer, and ③ control layer. These layers rely on sensing, network [3], processing of complex algorithms, and actuation implemented by electrical and/or electronic (E/E) systems. This study focuses on the planning and control layers of the AV system, which assumes that the perception layer works satisfactorily.

With the increase of advanced functionalities included in AVs, safety during their operational phase is of paramount importance for the road vehicles industry. However, there have been several

fatal accidents involving AVs [4,5], which underscore the importance and urgency of guaranteeing their safety. The reasons for the above accidents can be attributed to three typical safety issues faced by AVs: ① functional safety (ISO 26262) [6], ② safety of the intended functionality (SOTIF, ISO 21448) [7], and ③ cybersecurity (ISO 21434) [8]. Among these three, the SOTIF stands out as both a current academic research hotspot and an immediate challenge for AV applications. The SOTIF aims to handle potentially hazardous behaviors (PHBs), including insufficiencies or limitations related to the specifications, performance, and situational awareness, with or without reasonably foreseeable misuse, and surrounding impacts (e.g., other users, passive infrastructure, weather, and electromagnetic interference).

Given this consideration, this study deduced that the current motion planning and control techniques also suffer from issues that fall within the scope of the SOTIF. For example, uncertainties such as model mismatches will inevitably lead to control errors in the future while the planning layer does not consider the impact of these errors within the planning cycle. Moreover, AVs are affected by environmental uncertainty, and their actuators and sensors have performance limitations.

* Corresponding author.

E-mail address: ynli@cqu.edu.cn (Y. Li).

<https://doi.org/10.1016/j.eng.2023.12.003>

2095-8099/© 2024 THE AUTHORS. Published by Elsevier LTD on behalf of Chinese Academy of Engineering and Higher Education Press Limited Company. This is an open access article under the CC BY-NC-ND license (<http://creativecommons.org/licenses/by-nc-nd/4.0/>).

Fig. 1(a) shows an example scenario where uncertainties may lead to PHBs in automated driving. To date, however, most research on motion planning and control has not fully considered these uncertainties, and the desired trajectory is generally optimized individually by the planning layer. Therefore, as shown in Fig. 1(b), the main focus of this study is to reduce the possible hazardous/unknown areas in automated driving scenario categories. Specifically, this study generates and tracks a trajectory that can avoid obstacles and corresponding uncertainties, and mitigate unavoidable crashes.

1.2. Related work

The planning layer is the core that directly impacts driving safety. This layer is responsible for deciding the optimal driving behavior and generating a collision-free local trajectory to be followed at each instant. Heuristic approaches, including A* [9], Dijkstra [10], and rapidly exploring random tree (RRT) [11], were first applied to robot path planning. However, the heuristic approaches have difficulty generating smooth trajectories with continuous curvature. Therefore, curve-based methods, including the polynomial [12], Bezier-based [13], spline curve [14], and generation-selection-based [15] methods, were utilized to generate smooth trajectories. The quintic polynomials were proved as the jerk-optimal connections between a start state and an end state [12]. Moreover, the curve-based methods require a further assessment of the generated trajectories to select the optimal trajectory. Therefore, optimization-based methods, such as artificial potential field (PF) method [16], can be used to obtain smooth and curvature continuous trajectories. Nevertheless, the trajectories generated by the PF and gradient descent methods may converge toward local minima, resulting in rough and unexpected trajectories. Additionally, some artificial intelligence (AI)-based motion planning methods using historical data have emerged recently, such as reinforcement learning (RL) and deep learning (DL) [17]. The AI-based techniques are challenging to interpret and require high hardware costs for online applications. Considering the trade-off between computational cost and optimality, this study uses a quintic polynomial for smooth curve constructions and a PF function considering the obstacle sizes for discrete assessment.

The control layer is the core that directs the AV's actuators to follow the reference trajectories optimized by the planning layer. State-of-the-art approaches, such as dynamical game-based control [18], robust control [19], optimal control [20], RL-based control [21], and model predictive control (MPC) [22–24], are commonly applied to trajectory-tracking tasks. The main disadvantage of most of these approaches is that the AV's critical safety and actua-

tor constraints are not explicitly considered. Moreover, robust control can be computationally intensive and behaves too conservatively, whereas RL-based control requires improved interpretability. By contrast, MPC has been extensively studied and applied to AV systems owing to its ability to systematically exploit prediction information and handle multiple-input multiple-output (MIMO) under constraints.

Nevertheless, the traditional MPC could not handle uncertainties such as model mismatches and sensor noises. Therefore, schemes considering the impact of uncertainties in future evolution were studied. The common approaches are robust MPC (RMPC) [25] with a bounded set description and stochastic MPC (SMPC) with a probabilistic description [26]. However, it should be noted that uncertainties such as model mismatches are difficult to describe using probability. Hence, we consider the RMPC more promising than the SMPC in AV control tasks.

The RMPC schemes address all possible uncertainties by considering the worst case. Min-max RMPC [27] was first proposed by solving dynamical programming (DP) at each time step; however, it is computationally expensive. Subsequently, a more efficient tube-based RMPC (TRMPC) [28] was developed to guarantee the robustness and stability of the constraint satisfaction with a lower computational cost. The TRMPC scheme creates a condition similar to the real state being tightened in a tube. Compared to the traditional MPC, the online computational burden of the TRMPC is slightly increased.

Therefore, the TRMPC scheme has been applied widely in the AV control field, such as lateral control for AVs [29], trajectory tracking for autonomous race cars [30], active safety control for four-wheel steering [31], fault-tolerant control [32], and platoon control [33].

However, traditional TRMPC also faces difficulties in practical applications. For example, the high cost of set operations often limits computation to only a few time steps, which prevents the evaluation of the uncertainties in future evolution.

1.3. Contribution

Inspired by the existing literature on motion planning and control, the main contribution of this study is to propose a safe motion planning and control (SMPAC) framework for AVs to guarantee the safety of automated driving under multi-dimensional uncertainties. Fig. 2 shows the overall schematic of the study.

The core idea of SMPAC can be summarized as follows:

- (1) For the control layer, we develop a flexible zonotopic TRMPC (FTMPC) controller by leveraging an efficient reachability analysis on the uncertainties. The controller can converge the future evolution of all possible uncertainties into a minimal robust positive invariant (mRPI) set.
- (2) For the planning layer, we propose a concept of safety sets, which describes the geometric boundaries that ego vehicle/obstacles may reach by considering the bounded multi-dimensional uncertainties from the control layer. The safety sets guarantee that the real trajectories of the ego vehicle are always constrained in a safety tube.

Furthermore, the proposed SMPAC is a general scheme with interchangeable planning methods. Therefore, we believe that SMPAC has potential applications in other robotic systems, including but not limited to mobile robots and unmanned underwater vehicles.

1.4. Paper organization

The remainder of this study is presented as follows. Section 2 introduces the preliminaries for the set operations and zonotopes. In section 3, the dynamic model with uncertainties is developed,

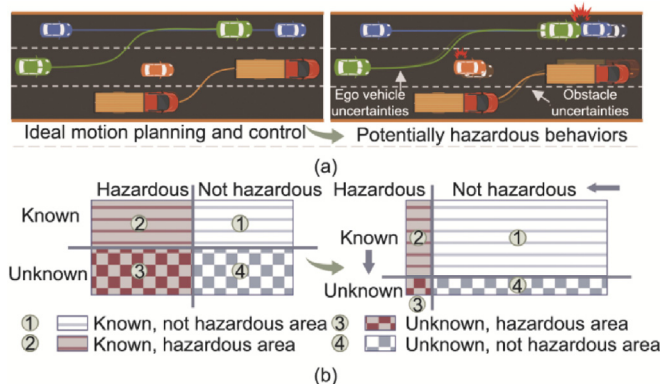


Fig. 1. Motivation. (a) Example of PHBs. (b) Evolution of scenario categories resulting from SOTIF.

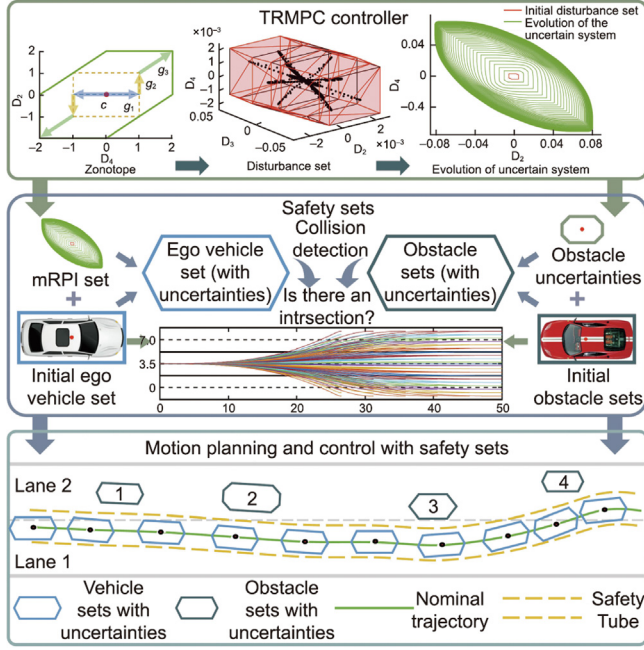


Fig. 2. Schematic of the overall block diagram.

and the FTMPC scheme is proposed. Section 4 presents the motion planning approach with safety sets to cope with multi-uncertainties. The co-simulations (MATLAB/Simulink, R2021b, MathWorks, USA; CarSim, 2019 version, Mechanical Simulation Corporation, USA) and hardware-in-the-loop experiments (HIL) performed to validate the proposed SMPAC are described in section 5. Finally, the conclusions are summarized in section 6.

2. Preliminaries

2.1. Definition of set operations

This study revolves around a set theory, hence the following three basic set operations are introduced first.

For a linear matrix $\mathbf{L} \in \mathbb{R}^{n \times n}$, sets $\mathbb{S}_1, \mathbb{S}_2 \subset \mathbb{R}^n$, and elements $s_1, s_2 \in \mathbb{R}^n$,

Linear map:

$$\mathbf{L}\mathbb{S}_1 = \{\mathbf{L}s_1 | s_1 \in \mathbb{S}_1\} \quad (1)$$

Minkowski sum:

$$\mathbb{S}_1 \oplus \mathbb{S}_2 = \{s_1 + s_2 | s_1 \in \mathbb{S}_1, s_2 \in \mathbb{S}_2\} \quad (2)$$

Pontryagin difference:

$$\mathbb{S}_1 \ominus \mathbb{S}_2 = \{s_1 | s_1 \oplus \mathbb{S}_2 \subseteq \mathbb{S}_1\}. \quad (3)$$

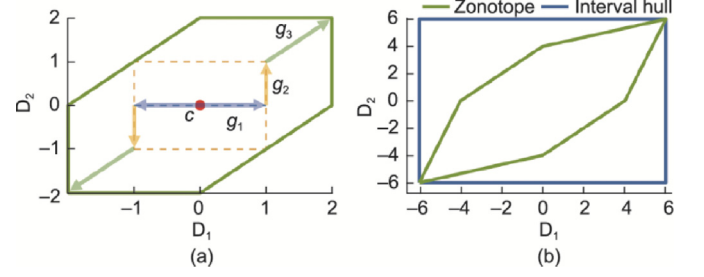
2.2. Zonotopes

A bounded polyhedral set is a polytope. The zonotope shown in Fig. 3 (a) is a class of centrally-symmetric polytopes.

The zonotope is also an affine transformation of the hypercube. An n -order zonotope ($\mathbb{Z} \subset \mathbb{R}^n$) transformed from an s -order hypercube ($\mathbb{B}^s \subset \mathbb{R}^s$) is described by

$$\mathbb{Z} = \mathbf{c} \oplus \mathbf{G}\mathbb{B}^s = \{\mathbf{c} + \mathbf{G}\boldsymbol{\varepsilon} | \boldsymbol{\varepsilon} \in \mathbb{B}^s, \mathbb{B}^s = [-1, 1]^s\}, \quad (4)$$

where $\mathbf{c} \in \mathbb{R}^n$ is the center and $\mathbf{G} = [\mathbf{g}_1, \mathbf{g}_2, \dots, \mathbf{g}_s] \in \mathbb{R}^{n \times s}$ is the generator. In this study, the zonotope is abbreviated as $\mathbb{Z} = \langle \mathbf{c}, \mathbf{G} \rangle$.


 Fig. 3. Construction of a zonotope, for example, $\mathbf{c} = [0; 0]$, $\mathbf{g}_1 = [1; 0]$, $\mathbf{g}_2 = [0; 1]$, $\mathbf{g}_3 = [1; 1]$. (b) Interval hull of a zonotope. D: Dimension, D_i is the i -th dimension.

Moreover, zonotopes hold the following essential properties.

For $\mathbf{c}_1, \mathbf{c}_2 \in \mathbb{R}^n$, $\mathbf{G}_1, \mathbf{G}_2 \in \mathbb{R}^{n \times s}$, the linear map and Minkowski sum of two zonotopes are computed by

$$\mathbf{L}\langle \mathbf{c}, \mathbf{G} \rangle = \langle \mathbf{L}\mathbf{c}, \mathbf{L}\mathbf{G} \rangle, \quad (5)$$

$$\langle \mathbf{c}_1, \mathbf{G}_1 \rangle \oplus \langle \mathbf{c}_2, \mathbf{G}_2 \rangle = \langle \mathbf{c}_1 + \mathbf{c}_2, [\mathbf{G}_1, \mathbf{G}_2] \rangle. \quad (6)$$

The Frobenius norm of the generator denotes the size of the zonotope $\mathbb{Z} = \langle \mathbf{c}, \mathbf{G} \rangle$:

$$F_r(\mathbb{Z}) = \|\mathbf{G}\|_F = \sqrt{\text{trace}(\mathbf{G}^T \mathbf{G})}. \quad (7)$$

The interval hull $\square \mathbb{Z}$ of a zonotope \mathbb{Z} is computed by

$$\square \mathbb{Z} = \mathbf{c} \oplus rs(\mathbf{G})\mathbb{B}^n, \quad (8)$$

where $rs(\mathbf{G})$ a diagonal matrix such that $rs(\mathbf{G})_{ii} = \sum_{j=1}^s |\mathbf{G}_{ij}|$, $i = 1, \dots, n$. Fig. 3 (b) illustrates the geometric interpretation of the interval hull $\square \mathbb{Z}$.

The P -radius of a zonotope \mathbb{Z} is defined by

$$P_r(\mathbb{Z}) = \max_{\mathbf{z} \in \mathbb{Z}} (\|\mathbf{z} - \mathbf{c}\|_P^2), \quad (9)$$

where $\mathbf{P} = \mathbf{P}^T \succ 0$ is a symmetric and positive definite matrix. \mathbf{P} is set as the identity matrix in this study, such that $\sqrt{P_r(\mathbb{Z})}$ represents the Euclidean distance.

Furthermore, all defined sets in this study are represented by zonotopes. The main reasons are summarized as follows:

- (1) Zonotopes guarantee that all sets defined in this study are compact, convex, and contain the origin in their interior.
- (2) The zonotopic set operations in Eqs. (5) and (6) enable an exact, fast, and visual exploration of the system evolution in the FTMPC scheme.
- (3) Table 1 illustrates that the zonotopes provide higher accuracy than ellipsoids while having lower time complexity than polytopes [34].

Table 1

Accuracy: e denotes exact computation, o denotes outer approximation; time complexity $O(\cdot)$: $-$ denotes that it is determined by methods. n is the order of the set representation.

| Set Representation | Linear Map | Minkowski Sum |
|----------------------|-----------------|-----------------|
| Half-space Polytopes | $e, O(n^3)$ | $e, O(2^n)$ |
| Vertex Polytopes | $e, O(n^2 2^n)$ | $e, O(n^2 2^n)$ |
| Ellipsoids | $e, O(n^3)$ | $o, -$ |
| Zonotopes | $e, O(n^3)$ | $e, O(n)$ |

3. Flexible zonotopic TRMPC scheme

The FTMPC controller for uncertainties is introduced in this section. The process includes modeling the AV and uncertainties, determining known constraints, evaluating the evolution of the uncertain system, and developing a varying zonotopic tube.

3.1. Dynamics and uncertainties modeling for AV

3.1.1. 3-degree of freedom vehicle model

Considering the trade-off between the model accuracy and computational cost, a simplified vehicle model consisting of a 1-degree of freedom (1-DOF) longitudinal model and a 2-DOF bicycle model is used under certain assumptions [35]. Fig. 4 depicts the vehicle model with the longitudinal, lateral, and yaw dynamics governed by

$$\begin{cases} m(\dot{v}_x - v_y\dot{\psi}) = F_{xT} \\ m(\dot{v}_y + v_x\dot{\psi}) = F_{yf}\cos\delta + F_{xf}\sin\delta + F_{yr} \\ I_z\ddot{\psi} = F_{yf}l_f\cos\delta + F_{xf}l_f\sin\delta - F_{yr}l_r, \end{cases} \quad (10)$$

where XOY is the inertial coordinate system for the ground and xoy is the vehicle coordinate system. For the xoy body-fixed coordinates, m is the vehicle mass, l_f and l_r are the front and rear wheelbase, I_z is the moment of inertia through the center of gravity about the yaw axis, v_x and v_y are the vehicle's longitudinal and lateral velocities, ψ is the vehicle heading angle, δ is the steering angle of the front wheels, F_{xT} is the total longitudinal tire force, and F_{xi} and F_{yi} ($i = \{f, r\}$) are the longitudinal and lateral forces of the front/rear tires, respectively.

Assuming that the lateral acceleration a_y and vehicle sideslip angle β are small, and the vertical tire load is constant, for simplicity, the lateral tire forces F_{yf} and F_{yr} are considered to be linear with the tire slip angles α_f (front tire) and α_r (rear tire):

$$\begin{cases} F_{yf} = c_f\alpha_f \\ F_{yr} = c_r\alpha_r \\ \alpha_f = \delta - \frac{(l_f\dot{\psi} + v_y)}{v_x} \\ \alpha_r = \frac{(l_r\dot{\psi} - v_y)}{v_x}, \end{cases} \quad (11)$$

where c_f and c_r are the corner-stiffnesses of the front and rear tires, respectively.

3.1.2. Error model for trajectory tracking

Leveraging an error model is a more effective approach for tracking a pre-planned trajectory. As shown in Fig. 5, e_v , e_y , and e_ψ are the tracking errors of the longitudinal velocity, lateral distance, and heading angle with respect to the reference trajectory,

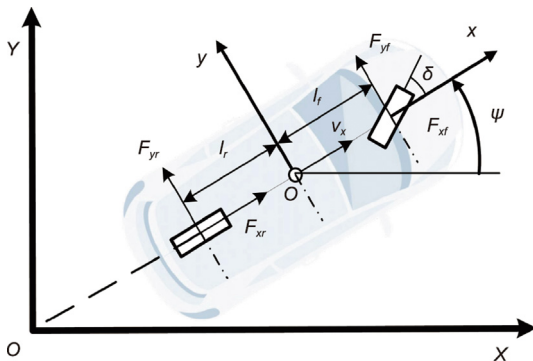


Fig. 4. 3-DOF vehicle model.

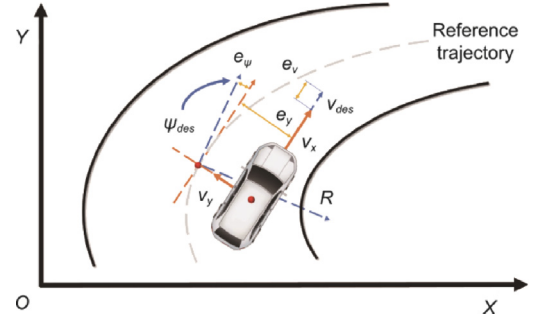


Fig. 5. Error model for trajectory tracking.

respectively. According to the kinematic relationship, \dot{e}_v , \dot{e}_y , \dot{e}_ψ , \ddot{e}_v , \ddot{e}_y , and \ddot{e}_ψ are defined as

$$\begin{cases} \dot{e}_v = \frac{F_{xT}}{m} + v_y\dot{\psi} - \dot{v}_{x,des} \\ \dot{e}_y = v_y + v_x e_\psi \\ \dot{e}_\psi = \dot{\psi} - \dot{\psi}_{des} \\ \ddot{e}_v = \ddot{v}_x \\ \ddot{e}_y = \ddot{v}_y \\ \ddot{e}_\psi = \ddot{\psi}, \end{cases} \quad (12)$$

where $\dot{v}_{x,des} = v_{y,des}\dot{\psi}_{des} + a_{x,des}$, $v_{y,des}$ is the desired lateral velocity, $a_{x,des}$ is the desired longitudinal acceleration, $\dot{\psi}_{des} = \frac{v_x}{R}$ is the desired yaw rate, and R is the radius of the reference trajectory.

According to the state variable dynamics in Eqs. (10) and (11), as well as the tracking error expression in Eq. (12), the continuous real AV model can be described as follows

$$\dot{\mathbf{x}}_e = \mathbf{A}_c \mathbf{x}_e + \mathbf{B}_1 \mathbf{u}_e + \mathbf{B}_2 \mathbf{w}_{des} + \mathbf{B}_3 \mathbf{w}_c \quad (13)$$

$$\mathbf{A}_c = \begin{bmatrix} 0 & 0 & 0 & 0 & 0 \\ 0 & 0 & 1 & 0 & 0 \\ 0 & 0 & -\frac{c_f+c_r}{m v_x} & \frac{c_f+c_r}{m} & -\frac{c_f l_f + c_r l_r}{m v_x} \\ 0 & 0 & 0 & 0 & 1 \\ 0 & 0 & -\frac{c_f l_f - c_r l_r}{I_z v_x} & \frac{c_f l_f - c_r l_r}{I_z} & -\frac{c_f l_f^2 + c_r l_r^2}{I_z v_x} \end{bmatrix} \quad (14)$$

$$\mathbf{B}_1 = \begin{bmatrix} \frac{1}{m} & 0 \\ 0 & 0 \\ 0 & \frac{c_f}{m} \\ 0 & 0 \\ 0 & \frac{c_f l_f}{I_z} \end{bmatrix}, \quad \mathbf{B}_2 = \begin{bmatrix} -1 & 0 \\ 0 & 0 \\ 0 & -v_x - \frac{(c_f l_f - c_r l_r)}{m v_x} \\ 0 & 0 \\ 0 & -\frac{(c_f l_f^2 + c_r l_r^2)}{I_z v_x} \end{bmatrix} \quad (15)$$

where $\mathbf{x}_e = [e_v, e_y, \dot{e}_y, e_\psi, \dot{e}_\psi]^T$ is the state, $\mathbf{u}_e = [F_{xT}, \delta]^T$ is the control input, and $\mathbf{w}_{des} = [\dot{v}_{x,des}, \dot{\psi}_{des}]^T$ denotes the information from the reference trajectory. The additive disturbance \mathbf{w}_c generalizes the internal and external uncertainties caused by all the adverse factors. Here, the internal uncertainties mainly include the coupled dynamics of longitudinal and lateral (the $v_y\dot{\psi}$ term in Eq. (12)) time-varying parameters, and unmodeled dynamics. The external uncertainties mainly include sensor noises and environmental disturbances. The disturbance matrix \mathbf{B}_3 is determined under scenarios encompassed by the operational design domain (ODD) of automated driving.

3.1.3. Zero steady-state error model

The presence of the $\mathbf{B}_2 \mathbf{w}_{des}$ term in Eq. (13) prevents the tracking errors from all converging to zero. Hence a feedforward term of the control inputs is designed to ensure a zero steady-state error.

The steady-state \mathbf{x}_{ss} and steady-input \mathbf{u}_{ss} are obtained by the final value theorem,

$$\begin{cases} \mathbf{x}_{ss} = [0, 0, 0, \frac{\rho l_f m v_x^2}{c_f l} - \rho l_r, 0]^T \\ \mathbf{u}_{ss} = [-m \dot{v}_{x,des}, \rho(l + K_V v_x^2)]^T \end{cases} \quad (16)$$

where $\rho = 1/R$ is the reference curvature, $l = l_f + l_r$ is the wheelbase, and $K_V = l_f m / c_f l - l_r m / c_r l$ is the understeer gradient.

Substitute Eq. (16) into Eq. (13) and define $\mathbf{x} = \mathbf{x}_e - \mathbf{x}_{ss}$, $\mathbf{u}_\Delta = \mathbf{u}_e - \mathbf{u}_{ss}$. The zero steady-state error model can be described by

$$\dot{\mathbf{x}} = \mathbf{A}_c \mathbf{x} + \mathbf{B}_1 \mathbf{u}_\Delta + \mathbf{B}_3 \mathbf{w}_c, \quad (17)$$

with the full-output $\mathbf{y} = \mathbf{C}_c \mathbf{x}$, $\mathbf{C}_c = \mathbf{I}_{n_x}$, \mathbf{I}_{n_x} is an identity matrix.

3.1.4. Real system

By the zero-order hold method, the discrete real AV system to be controlled can be expressed as

$$\mathbf{x}_k = \mathbf{A} \mathbf{x}_{k-1} + \mathbf{B} \mathbf{u}_{k-1} + \mathbf{w} \quad (18)$$

with the output $\mathbf{y}_k = \mathbf{C} \mathbf{x}_k$, where $\mathbf{x}_k \in \mathbb{R}^{n_x}$, $\mathbf{u}_k \in \mathbb{R}^{n_u}$, $\mathbf{A} = e^{\mathbf{A}_c T_s} \in \mathbb{R}^{n_x \times n_x}$, $\mathbf{B} = \int_0^{T_s} e^{\mathbf{A}_c t} dt \mathbf{B}_1 = \sum_{k=0}^{\infty} \frac{(\mathbf{A}_c)^k (T_s)^{k+1}}{(k+1)!} \mathbf{B}_1 \in \mathbb{R}^{n_x \times n_u}$, $\mathbf{w} = \int_0^{T_s} e^{\mathbf{A}_c t} dt \mathbf{B}_3 \mathbf{w}_c \in \mathbb{R}^{n_w}$, $\mathbf{C} = \mathbf{C}_c \in \mathbb{R}^{n_y \times n_x}$, T_s is the sample time.

3.2. Zonotopic constraints of real system

Moreover, the real AV system in Eq. (18) is subject to zonotopic hard constraints, that is, $\forall k \in \mathbb{N}^+$, $\mathbf{x}_k \in \mathbb{X} = \langle \mathbf{0}, \mathbf{G}_x \rangle \subseteq \mathbb{R}^{n_x}$, $\mathbf{u}_k \in \mathbb{U} = \langle \mathbf{0}, \mathbf{G}_u \rangle \subseteq \mathbb{R}^{n_u}$, and $\mathbf{w} \in \mathbb{W} = \langle \mathbf{0}, \mathbf{G}_w \rangle \subseteq \mathbb{R}^{n_w}$. The zonotope generators $\mathbf{G}_x \in \mathbb{R}^{n_x \times n_x}$ and $\mathbf{G}_u \in \mathbb{R}^{n_u \times n_u}$ are known matrices determined by the characteristics of the AV system, which include the following aspects:

Trajectory tracking constraints:

$$\begin{cases} |e_v| \leq e_v^{max} \\ |e_y| < \frac{1}{2}(r_w - r_v) \\ |e_\psi| \leq e_\psi^{max} \end{cases} \quad (19)$$

where r_w is the lane width, r_v is the width of the ego vehicle, e_v^{max} and e_ψ^{max} are the maximum values of the velocity errors (e_v) and heading angle errors (e_y), respectively.

Handling stability constraints: The vehicle sideslip angle β has the empirical constrained boundary and the yaw rate $\dot{\psi}$ has a limit:

$$\begin{cases} |\beta| = \left| \frac{v_y}{v_x} = \frac{1}{v_x} \dot{e}_y - e_\psi \right| \leq \arctan(0.02 \mu g) \\ |\dot{\psi}| = |\dot{e}_\psi + \dot{\psi}_{des}| \leq \frac{\mu_y g}{v_x} \end{cases} \quad (20)$$

where the tire-ground adhesion coefficient μ (lateral for μ_y) is assumed to be known for the controller, and g is the gravity acceleration.

Actuator constraints: The control inputs F_{xT} , δ and their increments ΔF_{xT} , and $\Delta \delta$ have boundaries:

$$\begin{cases} F_{xT}^{min} \leq F_{xT} \leq F_{xT}^{max}, \Delta F_{xT}^{min} \leq \Delta F_{xT} \leq \Delta F_{xT}^{max} \\ \delta^{min} \leq \delta \leq \delta^{max}, \Delta \delta^{min} \leq \Delta \delta \leq \Delta \delta^{max} \end{cases} \quad (21)$$

Furthermore, the disturbance \mathbf{w} consists of the internal disturbance $\mathbf{w}_{in} \in \mathbb{W}_{in}$ and the external disturbance $\mathbf{w}_{ex} \in \mathbb{W}_{ex}$, that is, $\mathbb{W} = \mathbb{W}_{in} \oplus \mathbb{W}_{ex}$. Here, \mathbf{w}_{in} can be determined by comparing the responses of the real model (CarSim model) and the nominal model in Eq. (22) within the ODD.

Fig. 6 (a)–(c) show the visual projection of \mathbb{W}_{in} in 3D and 2D views.

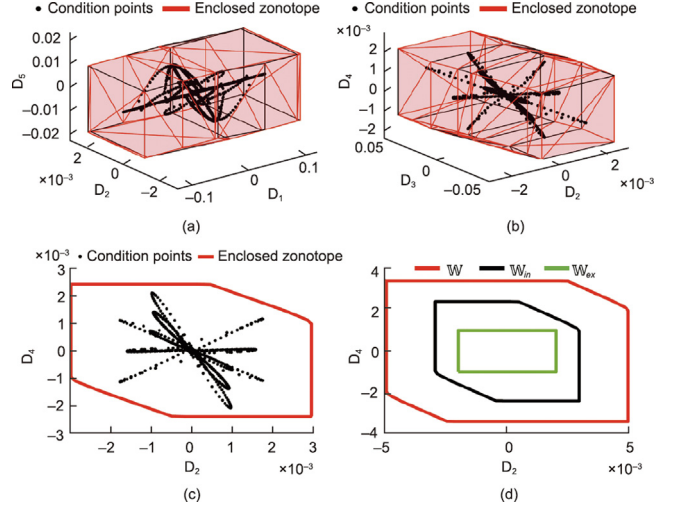


Fig. 6. Visual projection of zonotopes \mathbb{W} . (a) 3D view of internal disturbance set \mathbb{W}_{in} , D_1 - D_2 - D_3 . (b) 3D view of \mathbb{W}_{in} , D_2 - D_3 - D_4 . (c) 2D view of \mathbb{W}_{in} , D_2 - D_4 . (d) Relationship of disturbance set \mathbb{W} , internal disturbance set \mathbb{W}_{in} , and external disturbance set \mathbb{W}_{ex} , (D: Dimension).

Assuming that the \mathbf{w}_{ex} (e.g., sensor noise boundary) is known, the generator $\mathbf{G}_w \in \mathbb{R}^{n_x \times n_c}$ of the \mathbf{w} can be determined. Fig. 6 (d) shows the visual relationship of \mathbb{W} , \mathbb{W}_{in} , and \mathbb{W}_{ex} .

3.3. FTMPC control law and uncertainty evolution

The discrete-time real system in Eq. (18) satisfies the finite time controllability condition [36]. In this section, the real system is divided into a nominal system and an uncertain system, which are handled separately.

3.3.1. Nominal system

We extract the deterministic part of the real system in Eq. (18), and the nominal model without considering the disturbance \mathbf{w} is defined as

$$\hat{\mathbf{x}}_k = \mathbf{A} \hat{\mathbf{x}}_{k-1} + \mathbf{B} \hat{\mathbf{u}}_{k-1} \quad (22)$$

where all top marks $\hat{\cdot}$ represent the corresponding nominal variables. The nominal control input $\hat{\mathbf{u}}_k$ is obtained by solving an MPC optimization problem for the nominal dynamics.

3.3.2. Uncertain system

We remove the deterministic part (Eq. (22)) from the real system in Eq. (18), and the uncertain model composed of the disturbance \mathbf{w} can be obtained,

$$\tilde{\mathbf{x}}_k = \mathbf{A} \tilde{\mathbf{x}}_{k-1} + \mathbf{B} \tilde{\mathbf{u}}_{k-1} + \mathbf{w} \quad (23)$$

where $\tilde{\mathbf{x}}_k = \mathbf{x}_k - \hat{\mathbf{x}}_k$, $\tilde{\mathbf{u}}_k = \mathbf{u}_k - \hat{\mathbf{u}}_k$, and all top marks $\tilde{\cdot}$ represent the corresponding uncertain variables. The state feedback gain solved by the linear quadratic regulator (LQR) is used to guarantee the stability of the uncertain system, that is, $\mathbf{K} = \text{LQR}(\mathbf{A}, \mathbf{B})$, $\tilde{\mathbf{u}}_k = \mathbf{K} \tilde{\mathbf{x}}_k$. The FTMPC control law applied to the real system in Eq. (18) is then expressed as

$$\mathbf{u}_k = \hat{\mathbf{u}}_k + \mathbf{K} \tilde{\mathbf{x}}_k \quad (24)$$

Hence, the uncertain system in Eq. (23) is rewritten as a stable autonomous system:

$$\tilde{\mathbf{x}}_k = \mathbf{A} \tilde{\mathbf{x}}_{k-1} + \mathbf{w} \quad (25)$$

where the feedback gain matrix \mathbf{K} makes $\mathbf{A}' = \mathbf{A} + \mathbf{BK} \in \mathbb{R}^{n_x \times n_x}$ Schur stable.

3.3.3. mRPI and stability of the uncertain system

The future evolution law of the uncertain system is evaluated by leveraging the reachability analysis.

According to the zonotope properties in Eqs. (5) and (6), the evolution of the uncertain system (Eq. (25)), $\tilde{\mathbf{x}}_{k+h|k} \in \tilde{\mathbb{X}}_{k+h|k}$, $\tilde{\mathbf{u}}_{k+h|k} \in \tilde{\mathbb{U}}_{k+h|k}$, $\mathbf{0}$ refer to the zero matrix) with time steps $h \in N^+$ is revealed as:

$$\begin{cases} \tilde{\mathbf{x}}_{k+h|k} = (\mathbf{A}^h + \dots + \mathbf{A}' + \mathbf{I})\mathbf{w} \\ \tilde{\mathbb{X}}_{k+h|k} = \langle \mathbf{0}, (\mathbf{A}^h + \dots + \mathbf{A}' + \mathbf{I})\mathbf{G}_w \rangle \\ \tilde{\mathbf{u}}_{k+h|k} = \mathbf{K}\tilde{\mathbf{x}}_{k+h|k} \\ \tilde{\mathbb{U}}_{k+h|k} = \mathbf{K}\tilde{\mathbb{X}}_{k+h|k} \end{cases} \quad (26)$$

Proposition 1. The control law in Eq. (24) stabilizes the uncertain system in Eq. (23).

Proof 1. Fig. 7(a) draws all zonotopes of $\tilde{\mathbb{X}}_{k+h|k}$ in the finite horizon ($h = 1000$) with CORA [37] to visualize the evolution of the uncertain system in Eq. (23). In Fig. 7(a), the boundary lines of the zonotopes become denser as the time steps increase.

Moreover, based on the definition of the zonotope size in Eq. (7), the size change rate of the uncertain state constraints $\tilde{\mathbb{X}}_{k+h|k}$ is defined as

$$R_{k+h}^{\text{size}} = \frac{\|\tilde{\mathbb{X}}_{k+h+1|k}\|_F - \|\tilde{\mathbb{X}}_{k+h|k}\|_F}{\|\tilde{\mathbb{X}}_{k+h|k}\|_F}. \quad (27)$$

Fig. 7(b) shows that the R_{k+h}^{size} decreases with the time steps rapidly, which indicates that the difference between two adjacent zonotopes will quickly converge to zero.

Consequently, owing to the Schur matrix \mathbf{A}' , the uncertain states constraints $\tilde{\mathbb{X}}_{k+h|k}$ in Eq. (26) will converge rapidly in a bounded set (mRPI $\subseteq \mathbb{R}^{n_x}$). Hence, the $\mathbf{K}\tilde{\mathbf{x}}_k$ term in the control law (Eq. (24)) stabilizes the uncertain system in Eq. (23).

3.4. Flexible zonotopic tube for nominal system

According to the nominal model in Eq. (22), the prediction model of the nominal system over the prediction horizon N_p can be expressed as

$$\hat{\mathbf{x}}_k = \Psi_k \hat{\mathbf{x}}_k + \Theta_k \hat{\mathbf{u}}_k \quad (28)$$

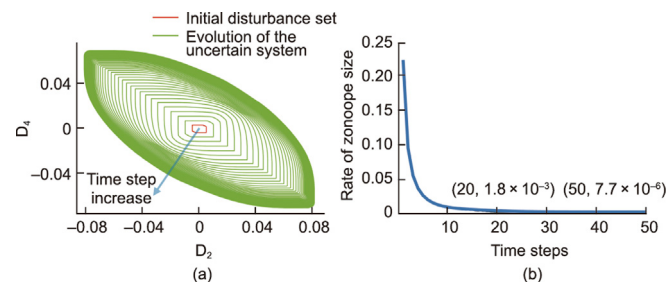


Fig. 7. Visual projection of mRPI (D_2 – D_4). (a) Evolution of uncertain system. (b) Size change rate R_{k+i}^{size} with time steps.

where N_c is the control horizon, $\Theta_k \in \mathbb{R}^{(n_x \times N_p) \times (n_u \times N_c)}$,

$$\begin{aligned} \Theta_k &= \begin{bmatrix} \mathbf{B} & \mathbf{0} & \dots & \mathbf{0} \\ \vdots & \vdots & \ddots & \vdots \\ \mathbf{A}^{N_c-1}\mathbf{B} & \mathbf{A}^{N_c-2}\mathbf{B} & \dots & \mathbf{B} \\ \vdots & \vdots & \ddots & \vdots \\ \mathbf{A}^{N_p-1}\mathbf{B} & \mathbf{A}^{N_p-2}\mathbf{B} & \dots & \mathbf{A}^{N_p-N_c}\mathbf{B} \end{bmatrix} \\ \Psi_k &= [\mathbf{A}, \dots, \mathbf{A}^{N_p}] \in \mathbb{R}^{(n_x \times N_p) \times n_x} \\ \hat{\mathbf{X}}_k &= [\hat{\mathbf{x}}_{k+1|k}^T, \dots, \hat{\mathbf{x}}_{k+N_p|k}^T]^T \in \mathbb{X}_k \subseteq \mathbb{R}^{(n_x \times N_p)} \\ \hat{\mathbb{X}}_k &= \langle \mathbf{0}, \hat{\mathbf{G}}_k^x \rangle = [\hat{\mathbb{X}}_{k+1|k}^T, \dots, \hat{\mathbb{X}}_{k+N_p|k}^T]^T \\ \hat{\mathbf{U}}_k &= [\hat{\mathbf{u}}_{k+1|k}^T, \dots, \hat{\mathbf{u}}_{k+N_c|k}^T]^T \in \hat{\mathbb{U}}_k \subseteq \mathbb{R}^{(n_u \times N_c)} \\ \hat{\mathbb{U}}_k &= \langle \mathbf{0}, \hat{\mathbf{G}}_k^u \rangle = [\hat{\mathbb{U}}_{k+1|k}^T, \dots, \hat{\mathbb{U}}_{k+N_c|k}^T]^T \end{aligned} \quad (29)$$

With the evolution of the $\tilde{\mathbb{X}}_{k+i|k}$ and $\tilde{\mathbb{U}}_{k+i|k}$, it yields that the MPC optimization problem for the nominal dynamics (nominal MPC) is subject to two tightened constraint sets, that is, $\tilde{\mathbb{X}}_k = \mathbb{X} \ominus \tilde{\mathbb{X}}_k$, $\tilde{\mathbb{U}}_k = \mathbb{U} \ominus \tilde{\mathbb{U}}_k = \mathbb{U} \ominus \mathbf{K}\tilde{\mathbb{X}}_k$.

Remark 1. According to Eq. (26), as the disturbance set \mathbb{W} increases, the uncertain constraint $\tilde{\mathbb{X}}_k$ increases, and the controller conservatism strengthens. If the disturbance set \mathbb{W} acts too significant, either $\mathbb{X} \ominus \tilde{\mathbb{X}}_k$ or $\mathbb{U} \ominus \mathbf{K}\tilde{\mathbb{X}}_k$ will be an empty set, rendering the controller unsolvable. For the \mathbb{W} determined in Subsection 3.2, the controller is sufficient.

To increase the quadratic programming (QP) feasible region of the nominal MPC and reduce conservatism, a flexible tube with varying cross-sections is designed at a negligible increase in computational cost [29]. The state and control tubes are parameterized with matrices $\hat{\mathbf{G}}_k^x$ and $\hat{\mathbf{G}}_k^u$ as

$$\begin{aligned} \hat{\mathbf{G}}_k^x &= \begin{bmatrix} \hat{\mathbf{G}}_{k+N_p|k} & \mathbf{A}^{N_p}\mathbf{G}_w & \dots & \mathbf{A}^3\mathbf{G}_w & \mathbf{A}^2\mathbf{G}_w \\ \hat{\mathbf{G}}_{k+N_p|k} & \mathbf{A}^{N_p}\mathbf{G}_w & \dots & \mathbf{A}^3\mathbf{G}_w & \mathbf{0} \\ \vdots & \vdots & \dots & \mathbf{0} & \mathbf{0} \\ \hat{\mathbf{G}}_{k+N_p|k} & \mathbf{A}^{N_p}\mathbf{G}_w & \mathbf{0} & \mathbf{0} & \mathbf{0} \\ \hat{\mathbf{G}}_{k+N_p|k} & \mathbf{0} & \mathbf{0} & \mathbf{0} & \mathbf{0} \end{bmatrix} \\ \hat{\mathbf{G}}_k^u &= \begin{bmatrix} \hat{\mathbf{G}}_{k+N_c|k}^u & \mathbf{K}\mathbf{A}^{N_c}\mathbf{G}_w & \dots & \mathbf{K}\mathbf{A}^3\mathbf{G}_w & \mathbf{K}\mathbf{A}^2\mathbf{G}_w \\ \hat{\mathbf{G}}_{k+N_c|k}^u & \mathbf{K}\mathbf{A}^{N_c}\mathbf{G}_w & \dots & \mathbf{K}\mathbf{A}^3\mathbf{G}_w & \mathbf{0} \\ \vdots & \vdots & \dots & \mathbf{0} & \mathbf{0} \\ \hat{\mathbf{G}}_{k+N_c|k}^u & \mathbf{K}\mathbf{A}^{N_c}\mathbf{G}_w & \mathbf{0} & \mathbf{0} & \mathbf{0} \\ \hat{\mathbf{G}}_{k+N_c|k}^u & \mathbf{0} & \mathbf{0} & \mathbf{0} & \mathbf{0} \end{bmatrix} \end{aligned} \quad (30)$$

where $\tilde{\mathbb{X}}_{k+N_p|k} = \mathbb{X} \ominus \tilde{\mathbb{X}}_{k+N_p|k} = \langle \mathbf{0}, \hat{\mathbf{G}}_{k+N_p|k}^x \rangle$, $\tilde{\mathbb{U}}_{k+N_c|k} = \mathbb{U} \ominus \mathbf{K}\tilde{\mathbb{X}}_{k+N_c|k} = \langle \mathbf{0}, \hat{\mathbf{G}}_{k+N_c|k}^u \rangle$.

The final optimization of the nominal MPC is expressed as

$$\begin{aligned} \min V_{N_p}(\hat{\mathbf{x}}_k, \hat{\mathbf{u}}_k) &= \hat{\mathbf{x}}_k^T \mathbf{Q}_c \hat{\mathbf{x}}_k + \hat{\mathbf{u}}_k^T \mathbf{R}_c \hat{\mathbf{u}}_k + \rho \varepsilon^2 \\ \text{s.t. } \hat{\mathbf{x}}_k &\in \tilde{\mathbb{X}}_k, \hat{\mathbf{u}}_k \in \tilde{\mathbb{U}}_k \end{aligned} \quad (32)$$

where $\rho \in \mathbb{R}^{n_e \times n_e}$ is the weight matrix of slack ε , $\mathbf{Q}_c \in \mathbb{R}^{(n_x \times N_p) \times (n_x \times N_p)}$, and $\mathbf{R}_c \in \mathbb{R}^{(n_u \times N_c) \times (n_u \times N_c)}$ are the weight matrices. Additionally, the final zonotopic constraint can be transformed to half-space polytopic constraints by Eq. (4) to make the QP optimization faster and more efficient [38].

Proposition 2. The control law in Eq. (24) stabilizes the nominal system in Eq. (22).

Proof 2. The nominal system in Eq. (22) has been proved to be exponentially stable under the assumption that the initial nominal state $\hat{\mathbf{x}}_t$ at each sample time ($t > 0$) is optimized as a parameter of the control law [28]. The optimization problem is subject to a significant constraint of $\mathbf{x}_t \in \hat{\mathbf{x}}_t \oplus \text{mRPI}$, that is, the optimal initial nominal state $\hat{\mathbf{x}}_t^*$ and optimal control sequence $\hat{\mathbf{U}}_t^*$ at time t are computed by

$$\left(\hat{\mathbf{x}}_t^*, \hat{\mathbf{U}}_t^* \right) = \arg \min_{\hat{\mathbf{x}}_t, \hat{\mathbf{U}}_t} \left\{ V_{N_p}(t) | \hat{\mathbf{U}}_t \in \hat{\mathbf{U}}_t, \mathbf{x}_t \in \hat{\mathbf{x}}_t \oplus \text{mRPI} \right\} \quad (33)$$

In this study, $\hat{\mathbf{x}}_t$ is derived from the real state and control input of the previous time step to measure the uncertain state $\tilde{\mathbf{x}}_t$ and determine the internal disturbance set in subsection 3.2, that is, $\hat{\mathbf{x}}_t = \mathbf{A}\mathbf{x}_{t-1} + \mathbf{B}\mathbf{u}_{t-1}$. The uncertain state $\tilde{\mathbf{x}}_t$ at time t satisfies that $\tilde{\mathbf{x}}_t = \mathbf{x}_t - \hat{\mathbf{x}}_t = \mathbf{w} \in \mathbb{W}$. The real state \mathbf{x}_t at time t also satisfies the above significant constraint, that is, $\mathbf{x}_t = \hat{\mathbf{x}}_t + \mathbf{w} \in \hat{\mathbf{x}}_t \oplus \mathbb{W} \subset \hat{\mathbf{x}}_t \oplus \text{mRPI}$. Hence the nominal MPC term (Eq. (32)) in the control law (Eq. (24)) stabilizes the nominal system in Eq. (22).

4. Motion planning with safety sets

This section introduces a motion planning algorithm that considers uncertainties in the Frenet Frame. The process consists of safety sets, trajectory generation, ranking, and collision detection.

4.1. Safety sets

Because the uncertain system evolution is demonstrated by reachability analysis in subsection 3.3, the mRPI can effectively describe all possible uncertainties caused by the tracking layer of the ego vehicle. Moreover, the uncertain areas of the mRPI may cause a potential collision. Therefore, a concept of safety sets is proposed to describe the geometric boundaries that the ego vehicle and obstacles may reach. The safety sets will be developed and applied in subsequent planning sections to guarantee motion planning security.

4.1.1. Ego vehicle set

Assuming that the effects of the acceleration variables are ignored, the safety set of the ego vehicle mainly considers the shape, location, and heading angle ψ .

(1) Shape and location: The ego vehicle's shape and location set \mathbb{V}_{sl} consists of the physical dimension set \mathbb{V}_{pd} and the uncertainty of the tracking errors mRPI₁₂.

For the former \mathbb{V}_{pd} , the zonotope shown in Fig. 8 (a) is used to enclose the physical dimension of the stationary ego vehicle. This zonotope is defined as the physical dimension set $\mathbb{V}_{pd} \subseteq \mathbb{R}^2$, which can effectively represent the original shape and location of the ego vehicle.

For the latter, the vehicle tracking errors are constrained by the first and second dimensions of the mRPI set, a result emanating from the introduced FTMPIC in section 3. Accordingly, mRPI₁₂ is defined as the reachable set of the ego vehicle's longitudinal and lateral tracking errors. The reachable set can be computed within

a finite safety horizon N_{safe} or an infinite horizon based on the evolution of the uncertain system.

Therefore, $\mathbb{V}_{sl} = \mathbb{V}_{pd} \oplus \text{mRPI}_{12} = \langle \mathbf{c}_e, \mathbf{G}_{sl} \rangle \subseteq \mathbb{R}^2$. Fig. 8 (b) shows the visual relationship of the mRPI₁₂, the original vehicle set \mathbb{V}_{pd} , and the shape and location set \mathbb{V}_{sl} .

(2) Heading angle ψ : The heading angle should be considered in the ego vehicle set when the ego vehicle is driving. Therefore, a rotation matrix is introduced to modify the generator \mathbf{G}_{sl} of the \mathbb{V}_{sl} :

$$\mathbf{R}_m(\psi) = \begin{bmatrix} \cos\psi & -\sin\psi \\ \sin\psi & \cos\psi \end{bmatrix} \quad (34)$$

As shown in Fig. 9 (a), the rotation function $\mathbf{R}_m(\psi)$ should modify the generator of \mathbb{V}_{sl} without changing its center. Thus, the ego vehicle set with a heading angle ψ can be represented by the matrix multiplication of the rotation matrix $\mathbf{R}_m(\psi)$ and the generator \mathbf{G}_{sl} , that is, $\langle \mathbf{c}_e, \mathbf{R}_m(\psi)\mathbf{G}_{sl} \rangle$.

Remark 2. Moreover, the heading angle error e_ψ is constrained by the fourth dimension of the mRPI, that is, $e_\psi^{\min} \leq e_\psi \leq e_\psi^{\max}$. Therefore, the ego vehicle set with the heading angle error \mathbb{V}_{e_ψ} can be simplified as the union of $\mathbb{V}_{e_\psi}^{\min}$ and $\mathbb{V}_{e_\psi}^{\max}$:

$$\mathbb{V}_{e_\psi} = \langle \mathbf{c}_e, \mathbf{R}_m(e_\psi^{\min})\mathbf{G}_{sl} \rangle \cup \langle \mathbf{c}_e, \mathbf{R}_m(e_\psi^{\max})\mathbf{G}_{sl} \rangle \quad (35)$$

Finally, \mathbb{V}_{e_ψ} is reduced to an interval hull $\square\mathbb{V}_{e_\psi}$ and $\square\mathbb{V}_{e_\psi}$ is rotated with the heading angle ψ . The ego vehicle set \mathbb{V}_s is obtained and shown in Fig. 9 (b).

4.1.2. Obstacle sets

The observation (or prediction) of the i -th ($i = 1, \dots, n_o$) obstacle (obs^i) by the ego vehicle has a bounded error [39], which can be described by an obstacle error set $\mathbb{O}_e^i \subseteq \mathbb{R}^{n_x}$. Similar to the process of the ego vehicle set, we first define a physical dimension set $\mathbb{O}_{pd}^i \subseteq \mathbb{R}^2$ for the i -th obstacle. Afterward, the i -th obstacle set with uncertainties $\mathbb{O}_s^i \subseteq \mathbb{R}^2$ can be computed with the obstacle

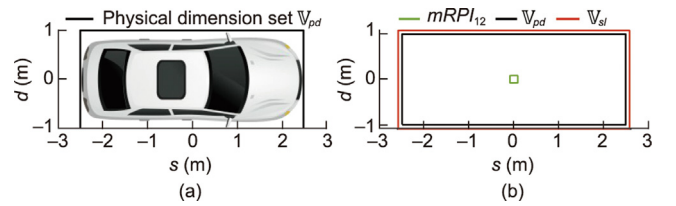


Fig. 8. Shape and location set of ego vehicle. (a) Physical dimension set \mathbb{V}_{pd} . (b) Relationship of mRPI₁₂, physical dimension set \mathbb{V}_{pd} , and shape and location set \mathbb{V}_{sl} .

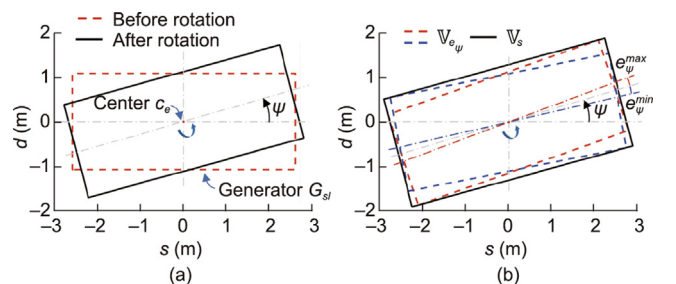


Fig. 9. Ego vehicle set. (a) Heading angle set with rotation function. (b) Relationship of ego vehicle set \mathbb{V}_s and heading angle error set \mathbb{V}_{e_ψ} .

physical dimension set \mathbb{O}_{in}^i , obstacle error set \mathbb{O}_e^i , and obstacle heading angle ψ_o^i .

4.2. Generation of candidate trajectories

In the Frenet coordinate system, the s -axis is set as the centerline of the rightmost lane, and the d -axis is perpendicular to the s -axis. The origin is merged with the origin of the Cartesian coordinate system and moves along the s -axis with the ego vehicle.

The quintic polynomial is proved as the jerk-optimal connection between the start state at t_0 and the end state at t_1 [12]. Therefore, the motions in the s and d directions are described by quartic and quintic polynomials:

$$\begin{cases} s(t) = a_0 + a_1 t + a_2 t^2 + a_3 t^3 + a_4 t^4 \\ d(t) = b_0 + b_1 t + b_2 t^2 + b_3 t^3 + b_4 t^4 + b_5 t^5, \end{cases} \quad (36)$$

where a_{0-4} and b_{0-5} are undetermined coefficients and t is the time. The start and end states are expressed as

$$\begin{cases} s(t_0), \dot{s}(t_0), \ddot{s}(t_0), d(t_0), \dot{d}(t_0), \ddot{d}(t_0) \\ \dot{s}(t_1), \ddot{s}(t_1), d(t_1), \dot{d}(t_1), \ddot{d}(t_1). \end{cases} \quad (37)$$

In addition, all the start states are set to be the same as the final vehicle state of the last control cycle to ensure continuity. The end states $\ddot{s}(t_1)$, $\dot{d}(t_1)$, and $\ddot{d}(t_1)$ are set to zero to ensure vehicle stability. Two sequences of the end velocity $\dot{s}(t_1)$ and the end d position $d(t_1)$ are designed to ensure that the candidate trajectories can cover all lanes. The following matrix equation is then obtained by taking an orthogonal combination of the two sequences of $\dot{s}(t_1)$ and $d(t_1)$:

$$\begin{cases} \mathbf{T}_1 \mathbf{P}_1 = \mathbf{S}_1, \mathbf{T}_1 \in \mathbb{R}^{5 \times 5}, \mathbf{P}_1 \in \mathbb{R}^{5 \times n_s}, \mathbf{S}_1 \in \mathbb{R}^{5 \times n_s}, \\ \mathbf{T}_2 \mathbf{P}_2 = \mathbf{S}_2, \mathbf{T}_2 \in \mathbb{R}^{6 \times 6}, \mathbf{P}_2 \in \mathbb{R}^{6 \times n_d}, \mathbf{S}_2 \in \mathbb{R}^{6 \times n_d}, \end{cases} \quad (38)$$

where \mathbf{T}_1 , \mathbf{P}_1 , \mathbf{S}_1 and \mathbf{T}_2 , \mathbf{P}_2 , \mathbf{S}_2 are presented in (Appendix A), respectively. The p -th ($p = 1, 2, \dots, n_s$) column of the matrix \mathbf{P}_1 corresponds to the polynomial parameters of $s(t)$ under the condition of $\dot{s}(t_1)^{(p)}$, and $0 \leq \dot{s}(t_1)^{(p)} \leq \dot{s}(t_1)^{max}$. The average acceleration $\frac{\dot{s}(t_1)^{(p)} - \dot{s}(t_0)}{t_1 - t_0}$ should satisfy comfortable acceleration limits. The q -th ($q = 1, 2, \dots, n_d$) column of the matrix \mathbf{P}_2 corresponds to the polynomial parameters of $d(t)$ under the condition of $d(t_1)^{(q)}$, and $d(t_1)^{(q)}$ should not exceed the road boundary.

As shown in Fig. 10, a cluster of the n_t candidate trajectories can be obtained by solving \mathbf{P}_1 and \mathbf{P}_2 , where $n_t = n_s \times n_d$.

4.3. Risk assessment and trajectory ranking

The candidate trajectories are discretely sampled and then ranked for risk assessment (J_{risk}), ride comfort (J_{com}), and trajectory stability (J_{sta}). The total cost function (J_{total}) is defined as

$$J_{total} = k_{risk} J_{risk} + k_{com} J_{com} + k_{sta} J_{sta}, \quad (39)$$

where k_{risk} , k_{com} , and k_{sta} are the corresponding weights.

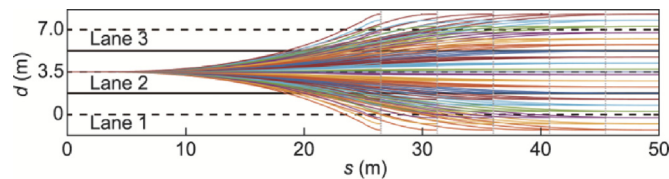


Fig. 10. Cluster of candidate trajectories.

4.3.1. Risk assessment

The risk assessment index J_{risk} is considered from two perspectives of road boundaries (crossable or non-crossable lane lines) and obstacles of various sizes (e.g., other vehicles, accidentally dropped cargo).

(1) Road boundary description: The periodic PF of the road boundaries U_{road} is generated by a trigonometric function to deal with multi-lane roads. The $U_{road} \in [0, 1]$, and can be written as

$$\begin{aligned} U_{road} &= \frac{1}{2} R_A(d) \left(\cos\left(\frac{2\pi d}{r_w}\right) + 1 \right) \\ R_A(d) &= p_m + \frac{1}{2} |\text{sgn}(d) + \text{sgn}(d - d_{cn})| (1 - p_m) \end{aligned} \quad (40)$$

where s and d are the Frenet coordinates of the ego vehicle, r_w is the lane width, $R_A(d)$ is the amplitude varying with d , $p_m \in [0, 1]$ denotes the risk value at the crossable edge lines, and d_{cn} is the d coordinate of the leftmost lane centerline. Fig. 11 shows the PF of the road.

(2) Obstacle description with the obstacle set \mathbb{O}_i^i : The i -th obstacle PF shown in Fig. 12(a) and (b) is generated by an exponential function. In which, the obstacle PF in Eq. (41) mainly considers the relative velocity $\Delta_v(i)$ and the obstacle size.

$U_{obs}(i) \in [0, 1]$, and can be written as

$$\begin{aligned} U_{obs}(i) &= \begin{cases} \exp\left(-\frac{D_{is}}{\Delta_v(i) + \epsilon}\right), & \Delta_v(i) \geq 0 \\ 0, & \Delta_v(i) < 0 \end{cases} \\ D_{is}(i) &= \left(\frac{s-s_i}{r_{is}}\right)^2 + \left(\frac{d-d_i}{l_{ieq}}\right)^2 \end{aligned} \quad (41)$$

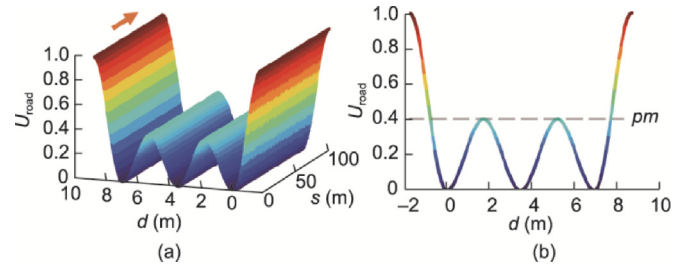


Fig. 11. PF of road U_{road} . (a) 3D view, $p_m = 0.4$. (b) 2D view, $p_m = 0.4$.

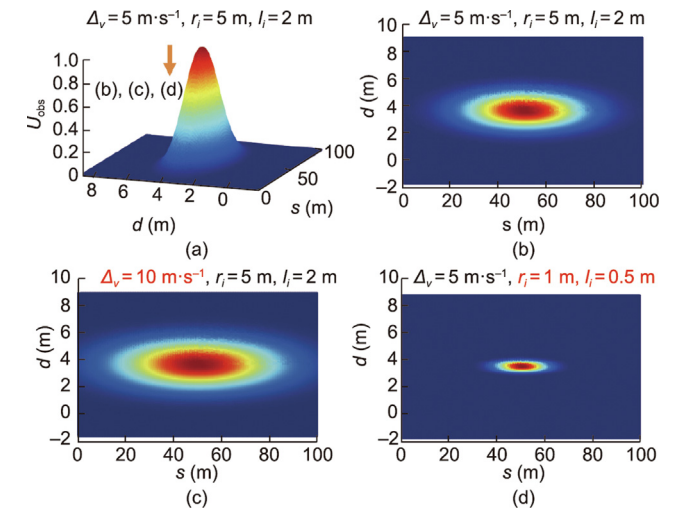


Fig. 12. PF of obstacles $U_{obs}(i)$. (a) 3D view, $\Delta_v = 5 \text{ m}\cdot\text{s}^{-1}$, $r_i = 5 \text{ m}$, $l_i = 2 \text{ m}$. (b) Top view, $\Delta_v = 5 \text{ m}\cdot\text{s}^{-1}$, $r_i = 5 \text{ m}$, $l_i = 2 \text{ m}$. (c) Top view, $\Delta_v = 10 \text{ m/s}$, $r_i = 5 \text{ m}$, $l_i = 2 \text{ m}$. (d) Top view, $\Delta_v = 5 \text{ m}\cdot\text{s}^{-1}$, $r_i = 1 \text{ m}$, $l_i = 0.5 \text{ m}$.

where $\epsilon = 0.0001$ is a safety coefficient formulated to prevent a singular value, $D_{is}(i)$ is a function of the relative distance, r_i and l_i are the width and length of the interval hull $\square \odot_s^i$ projection on the $s-d$ plane, respectively, and ϵ_s and ϵ_d are the shape and intensity parameters, respectively.

The worst-case caused by the velocity uncertainties of the ego vehicle and obstacle is considered. The possible maximum relative velocity $\Delta_v(i)$ is expressed by $\Delta_v(i) = v_x^{max} - v_i^{min}$. Here, $v_x^{max} = v_x + e_v^{max}$, e_v^{max} is constrained by the first dimension of the mRPI, v_i^{min} is the minimum obstacle velocity constrained by the corresponding dimension of the obstacle set \odot_e^i . Fig. 12 (c) shows that the higher the relative velocity, the stronger the PF energy.

Furthermore, an obstacle interval hull $\square \odot_s^i$ is used as the outer approximation of the obstacle set \odot_s^i by Eq. (8) to simplify the effect of the obstacle size on the obstacle PF. Fig. 12 (d) shows that the smaller the size, the weaker the PF energy.

Remark 3. The $U_{obs}(i)$ is set as a considerable fixed value when the perception layer determines that the obstacle is alive (human being or animal).

- (3) Risk assessment index J_{risk} : The PFs for all the discrete sample points in each trajectory are summed and then normalized to obtain the J_{risk} :

$$J_{risk} = \frac{\sum_{j=1}^{n_{sp}} (U_{road} + \sum_{i=1}^{n_o} U_{obs}(i))}{\max \sum_{j=1}^{n_{sp}} (U_{road} + \sum_{i=1}^{n_o} U_{obs}(i))}, \quad (42)$$

where n_{sp} is the number of discrete sample points and n_o is the number of obstacles.

4.3.2. Ride comfort

The ride comfort index J_{com} considers the curvature κ_j and the heading angle increments $\Delta\psi_j (j = 1, \dots, n_{sp})$ for all the discrete sample points:

$$J_{com} = \frac{\sum_{j=1}^{n_{sp}} (\kappa_j^2 + |\Delta\psi_j|)}{\max \sum_{j=1}^{n_{sp}} (\kappa_j^2 + |\Delta\psi_j|) + \epsilon}, \quad (43)$$

where $\kappa_j(t) = \frac{\dot{s}(t)\ddot{d}(t) - \dot{d}(t)\dot{s}(t)}{(\dot{s}^2(t) + \dot{d}^2(t))^{3/2}}$, $\Delta\psi_j = \psi_j - \psi(t_0)$, $\psi(t) = \arctan\left(\frac{\dot{s}(t)}{\dot{d}(t)}\right)$, and ϵ prevents a singular value.

4.3.3. Trajectory stability

The trajectory stability index J_{sta} considers the difference $(\Delta s_j, \Delta d_j)$ between the present candidate trajectories and desired trajectory of the last planning cycle to avoid the drastic change of the desired trajectory.

$$J_{sta} = \frac{\sum_{j=1}^{n_{sp}} (\Delta s_j^2 + \Delta d_j^2)}{\max \sum_{j=1}^{n_{sp}} (\Delta s_j^2 + \Delta d_j^2)} \quad (44)$$

4.4. Collision avoidance with safety sets

Although the cost function in subsection 4.3 considers the risk assessment, the trajectory does not impose a hard constraint on collision avoidance. In this section, efficient collision detection is achieved by determining the presence of intersections between the ego vehicle set \mathbb{V}_s and the obstacle sets \odot_s^i . Specifically, Algorithm 1 is adopted to reduce the computation burden of collision detection.

The candidate trajectories are detected in succession according to the ranking in subsection 4.3. The detection stops when there is

a collision-free trajectory. If there are collisions in all trajectories, the desired trajectory is optimized by another crash mitigation cost function J_{mit} at crash points.

$$J_{mit} = k_1 c_v + k_2 c_\theta + k_3 r_v, \quad (45)$$

where c_v is the crash speed, c_θ is the crash angle, r_v is the relative volume, and k_1 , k_2 , and k_3 are the corresponding weights. The crash angle is divided into full overlap collision, $\frac{1}{3}$ overlap near collision, and $\frac{2}{3}$ overlap collision [22].

The radii of the ego vehicle set R_v and the i -th obstacle R_o^i are computed by the P -radius of the zonotopes in Eq. (9). For n_{sp} discrete sample points of the trajectory being detected, all Euclidean distances $E_d(i, j)$ between the centers of the two sets $(\mathbb{V}_s$ and $\odot_s^i)$ are computed. The detection begins when the $E_d(i, j)$ is less than the sum of the vehicle radius and obstacle radius, that is, $E_d(i, j) \leq R_v + R_o(i)$.

Algorithm 1 (Algorithm for collision detection).

Input: Ranked candidate trajectories TRA(k)
 Output: Desired trajectory
 Initialize:
 $CI = \text{TRUE}$, $k = 0$, $R_v = P_r(\mathbb{V}_s)$, $R_o(i) = P_r(\odot_s^i)$
 while $CI = \text{TRUE}$ and $k \leq n_t$ do
 $CI \leftarrow \text{FALSE}$;
 for $i \leftarrow 1$ to n_o do
 for $j \leftarrow 1$ to n_{sp} do
 $E_d(i, j) \leftarrow$ center of ego vehicle and obs i ;
 if $E_d(i, j) \leq R_v + R_o(i)$ then
 $CI(i, j) \leftarrow \text{isintersection?}(\mathbb{V}_s, \odot_s^i)$;
 $CI = \text{OR}(CI, CI(i, j))$;
 end
 end
 end
 $k \leftarrow k + 1$;
 end
 if $CI = \text{FALSE}$ then
 return TRA(k)
 else
 Go to crash mitigation optimization in Eq. (45)
 end

After executing the process described in section 4, Fig. 13 shows an example of the MATLAB/Simulink result of trajectory planning without control at a specific time.

5. Results and discussion

In this section, a HIL experiment platform based on the simulation of MATLAB/Simulink and CarSim is conducted to validate the feasibility of the proposed SMPAC framework.

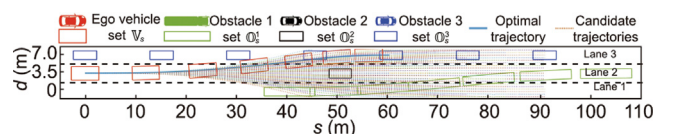


Fig. 13. Example of trajectory planning with safety sets.

5.1. HIL experiment validation

- (1) Experiment platform: The real-time performance of the SMPAC scheme is validated by a HIL experiment, in which “Simulink Desktop Real-time” provides the real-time environment. Fig. 14 (a) shows the schematic diagram of the HIL platform, and Fig. 14 (b) shows the physical connection. The host computer (i7-9700 K, Intel, USA) communicates with a mobile real-time target machine (M3, Speedgoat, Switzerland) and actuators with signal transmission components. The components include a control area network (CAN) card (Leaf Light v2, Kvaser, Sweden), a data acquisition

(DAQ) card (NI USB-6002, National Instruments, USA), a motor (86EBP159ALC, Shidaichaoqun, China), a motor driver (ZDM-2HA865, Shidaichaoqun, China), and a protocol conversion module (CAN to RS485, EBYTE, China).

- (2) Comparisons and test scenarios: The proposed SMPAC with the FTMPC controller is compared with a zero steady-state error TRMPC controller (ZMPC) and a zero steady-state error LQR controller (ZLQR) under the same framework. The zero steady-state error refers to the feedforward term in Eq. (16). The SMPAC framework provides decision-making, planning, and tracking for the ego vehicle. Table 2 summarizes the parameters of the SMPAC, including the vehicle, planner, and controller.

Moreover, two driving scenarios are constructed for validation and evaluation. Table 3 summarizes the information of the test scenarios, including the traffic participants, start states, and end states. Table 4 compares the tracking errors of the three controllers across the two scenarios.

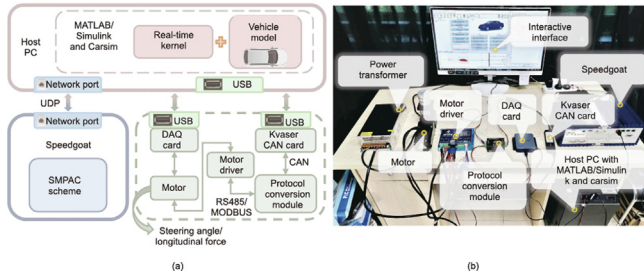


Fig. 14. Hardware-in-the-loop platform. (a) Schematic diagram. (b) Basic facilities.

Table 2 Parameters of SMPAC.

| Parameter | Definition | Value (unit) |
|-----------|---------------------------------|----------------------------|
| m | Vehicle mass | 1723 kg |
| I_z | Vehicle rotation inertia | 3234 kg·m ⁻² |
| l_f | Front wheelbase | 1.4 m |
| l_r | Rear wheelbase | 1.65 m |
| c_f | Front-wheel cornering stiffness | 65 000 N·deg ⁻¹ |
| c_r | Rear-wheel cornering stiffness | 50 000 N·deg ⁻¹ |
| T_{cs} | Controller sample Time | 0.02 s |
| T_{ps} | Planner sample Time | 0.1 s |

Table 3 Information of test scenarios.

| Scenario | Traffic participant | | Start state | | | | | End state | |
|------------|---------------------|-------|-------------|-----------|-----------|-----------|-------------------------------|------------------------------|-------------------------------|
| | Name | Type | Length (m) | Width (m) | s_0 (m) | d_0 (m) | v_{x0} (m·s ⁻¹) | Driving behavior | v_{x1} (m·s ⁻¹) |
| Scenario 1 | Ego vehicle | Car | 5 | 2 | 0 | 3.5 | 20 | Change from Lane-2 to Lane-3 | 24 |
| | Obstacle 1 | Truck | 10 | 1.72 | 60 | 0 | 15 | Change from Lane-1 to Lane-2 | 20 |
| | Obstacle 2 | Car | 4.5 | 1.68 | 60 | 3.5 | 0 | Stationary | 0 |
| | Obstacle 3 | Car | 4.5 | 1.68 | 0 | 7 | 25 | Uniform linear motion | 25 |
| Scenario 2 | Ego vehicle | Car | 5 | 2 | 0 | 3.5 | 20 | Collision avoidance | 18 |
| | Obstacle 1 | Truck | 10 | 1.72 | 60 | 0 | 15 | Change from Lane-1 to Lane-2 | 20 |
| | Obstacle 2 | Bike | 1.8 | 0.3 | 80 | 2.5 | 0 | Stationary | 0 |
| | Obstacle 3 | Car | 4.5 | 1.68 | 0 | 7 | 20 | Uniform linear motion | 20 |

Table 4 Tracking errors.

| Scenario | Controller | e_y (m) | e_ψ (°) | e_v (m·s ⁻¹) |
|----------|------------|---------------------------------|----------------|----------------------------|
| | | Mean, Max | Mean, Max | Mean, Max |
| 1 | FTMPC | 0.0179, 0.1807 | 0.2178, 3.594 | 0.0248, 0.0670 |
| | ZMPC | 0.0395, 0.4613 | 0.2709, 4.756 | 0.0451, 0.1266 |
| | ZLQR | 0.0773, 0.9205 | 0.5346, 13.42 | 0.0326, 0.1698 |
| 2 | FTMPC | 5.352×10^{-4} , 0.0033 | 0.0492, 0.2043 | 0.0271, 0.0652 |
| | ZMPC | 4.437×10^{-4} , 0.0026 | 0.0480, 0.2038 | 0.0424, 0.1101 |
| | ZLQR | 7.064×10^{-4} , 0.0044 | 0.0483, 0.2033 | 0.0211, 0.0492 |

Fig. 15(a)–(c) show the safety sets and trajectories of the proposed SMPAC with the FTMPC, ZMPC, and ZLQR schemes. The light blue lines denote the planned trajectories (without CarSim involved) of the ego vehicle at each planning cycle. The red points, green squares, and blue diamonds represent the real trajectories (with CarSim involved) of the ego vehicle, obstacle 2, and obstacle 3, respectively. Additionally, the safety sets of the ego vehicle and obstacles are drawn as zonotopes every second, where the different colors denote the different vehicles. Fig. 15(d) shows the partially enlarged view of Fig. 15(c). Fig. 15(e)–(g) show the planned velocities (light blue lines) and real velocities (red line) of the ego vehicle at each planning cycle. Fig. 15(h)–(n) show the comparison of the three controllers in the control inputs, tracking performances, and vital dynamic states of the ego vehicle. These indexes include the total longitudinal force, steering angle, lateral error, heading angle error, velocity error, yaw rate, and lateral acceleration.

In scenario 1, the ego vehicle decides to change from Lane-2 to Lane-3 to avoid collision with the stationary obstacle 2. The lane change process can be summarized in three steps. First, the ego vehicle deviates from the Lane-2 centerline to the Lane-3 boundary, decelerates to approximately $10 \text{ m}\cdot\text{s}^{-1}$, and prepares to change lanes. Second, after the surrounding vehicle (obstacle 3) passes, the ego vehicle completes the lane change and maintains the velocity

for a while. Finally, the ego vehicle adjusts its lateral position to the Lane-3 centerline and accelerates to approximately $25 \text{ m}\cdot\text{s}^{-1}$.

- (1) Safety satisfaction: As shown in Fig. 15(a)–(b), both SMPAC with FTMPC and ZMPC could avoid collision under uncertainties. Nevertheless, the proposed SMPAC with FTMPC keeps the ego vehicle farther away from obstacles and thus safer. In Fig. 15(c)–(d), it is observed that the ZLQR scheme exhibits PHBs because of the intersection of the ego vehicle set \mathbb{V}_s and obstacle 2 set \mathbb{O}_s^2 at 4.6 s. Consequently, the proposed SMPAC with FTMPC can guarantee safety at the handling limits, whereas conventional frameworks and controllers may exhibit PHBs.
- (2) Tracking performance: Fig. 15(h)–(n) and Table 4 both illustrate that FTMPC has the best tracking performance and vehicle stability among the three controllers at the handling limits and exhibits a significant improvement over ZMPC and ZLQR. Therefore, the proposed FTMPC has better robustness.

5.3. Scenario 2

Scenario 2 simulates that the ego vehicle faces an unlawful stationary bike (small non-crossable obstacle) ahead and two

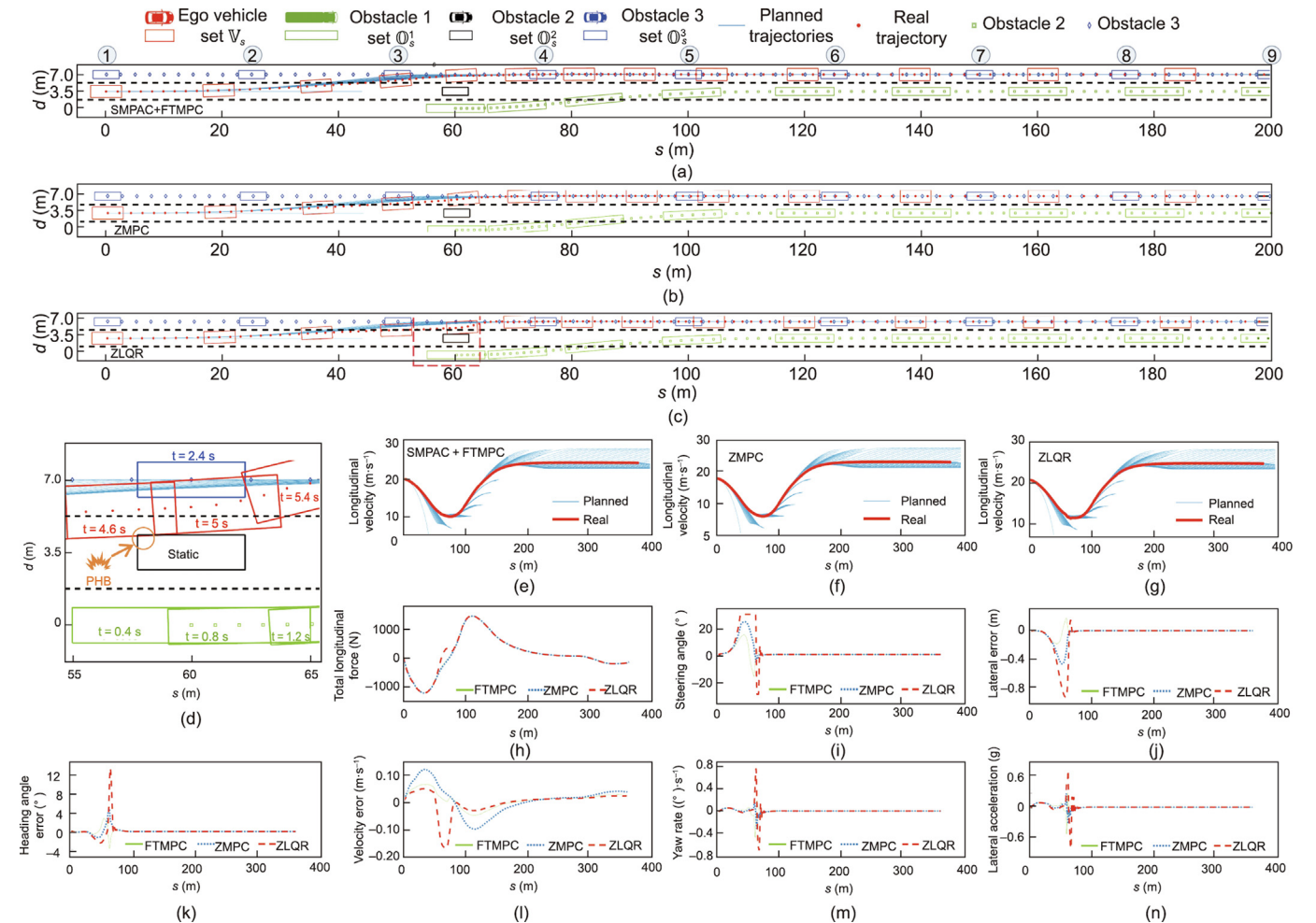


Fig. 15. Scenario 1: lane change at handling limits. (a) Safety sets and trajectories (SMPAC with FTMPC controller). (b) Safety sets and trajectories (ZMPC). (c) Safety sets and trajectories (ZLQR). (d) Partially enlarged view of (c). (e) Longitudinal velocity (SMPAC with FTMPC). (f) Longitudinal velocity (ZMPC). (g) Longitudinal velocity (ZLQR). (h) Total longitudinal force. (i) Steering angle. (j) Lateral tracking error. (k) Heading angle error. (l) Velocity error. (m) Yaw rate. (n) Lateral acceleration.

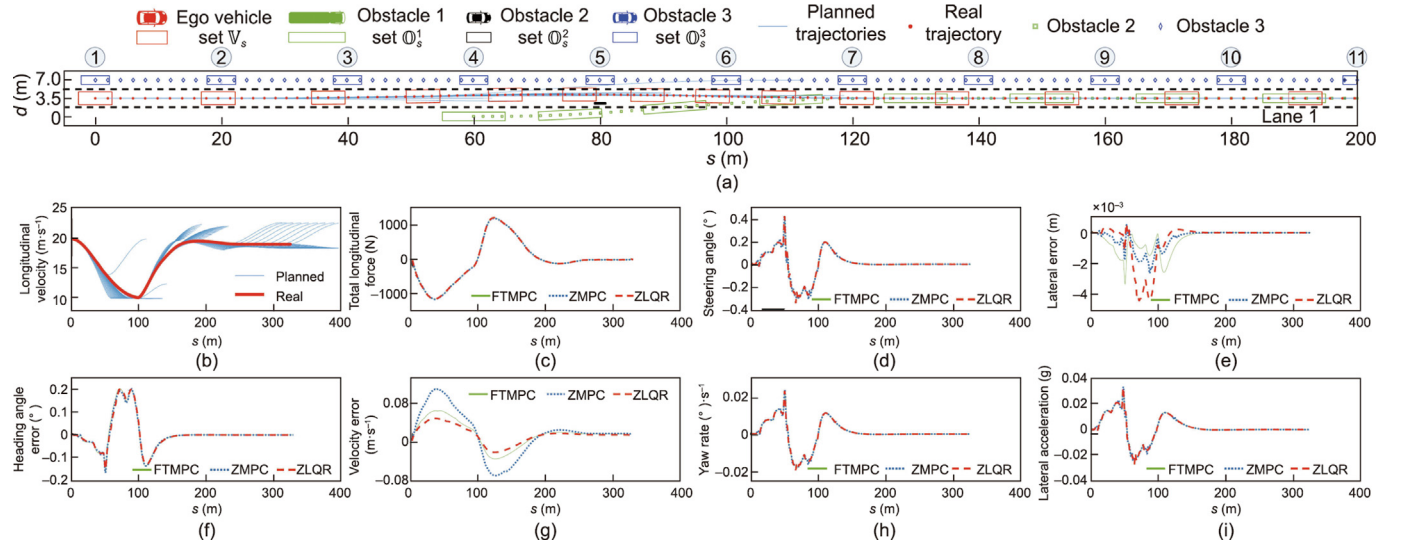


Fig. 16. Scenario 2: collision avoidance under normal conditions. (a) Safety sets and trajectories of all comparisons. (b) Longitudinal velocity of all comparisons. (c) Total longitudinal force. (d) Steering angle. (e) Lateral tracking error. (f) Heading angle error. (g) Velocity error. (h) Yaw rate. (i) Lateral acceleration.

surrounding vehicles in the left and right lanes. In this scenario, the vehicle is operating under normal conditions.

Specifically, as illustrated in Table 3, the ego vehicle is a car that initially drives along the centerline of Lane-2 at $20 \text{ m}\cdot\text{s}^{-1}$. Moreover, there are three obstacles. Obstacle 1 is a truck trying to change from Lane-1 (60 m) to Lane-2, with velocities of $15 \text{ m}\cdot\text{s}^{-1}$ and $20 \text{ m}\cdot\text{s}^{-1}$ before and after the lane change, respectively. Obstacle 2 is a stationary bike located 80 m in front of the ego vehicle and 1 m to the right of the Lane-2 centerline. Obstacle 3 is a car driving along the centerline of Lane-3 at a constant speed of $20 \text{ m}\cdot\text{s}^{-1}$.

Similar to scenario 1, Fig. 16 (a) shows the safety sets of the ego vehicle and obstacles every second. Fig. 16 (b) shows the planned and real velocities of the ego vehicle at each planning cycle. However, it is noteworthy that the trajectories of all the comparison groups in Fig. 16 (a) and (b) almost overlap, hence only one group is shown. Fig. 16 (c)–(i) show the control inputs, tracking performances, and vital dynamic states of the ego vehicle.

In scenario 2, the ego vehicle decides to deviate a little distance from the Lane-2 centerline toward the Lane-3 boundary to avoid collision with the stationary obstacle 2. The collision avoidance process can be summarized in three steps. First, the ego vehicle moves a distance away from the Lane-2 centerline to the Lane-3 boundary and gradually decelerates. Second, after avoiding obstacle 2, the ego vehicle returns to the Lane-2 centerline and decelerates to approximately $10 \text{ m}\cdot\text{s}^{-1}$. Finally, the ego vehicle drives along the Lane-2 centerline and accelerates to approximately $20 \text{ m}\cdot\text{s}^{-1}$.

- (1) Safety satisfaction: As shown in Fig. 16 (a) and (b), with the SMPAC framework, all three controllers are able to avoid collision under uncertainties. The differences between the three schemes are negligible. Therefore, the proposed SMPAC framework can guarantee safety under normal conditions.
- (2) Tracking performance: As shown in Fig. 16 (c)–(i) and Table 4, the tracking errors of FTMPC, ZMPC, and ZLQR are all minima owing to the feedforward term in Eq. (16). In addition, the differences between the three are almost negligible. Therefore, the proposed FTMPC has a high performance and less conservatism under normal conditions.

6. Conclusion

A SMPAC framework was proposed to address multi-dimensional uncertainties in autonomous driving. A dynamic model with multi-dimensional uncertainties was established for the control layer to accurately describe the real AV system. The FTMPC controller with the flexible tube was designed to guarantee robust stability and constrain the uncertain system in the bounded mRPI. For the planning layer, the safety sets were introduced to determine the geometric boundaries that the ego vehicle or obstacles possibly reach accordingly. The trajectory planning and collision avoidance with the safety sets were studied to reduce the PHBs caused by the uncertainties.

The HIL platform tested two types of scenarios: an active lane change scenario at the handling limits and a collision avoidance scenario under normal conditions. The results validated the safety, effectiveness, and real-time performance of the SMPAC scheme. Consequently, the SMPAC scheme can reduce possible hazardous/unknown areas in automated driving scenario categories for the SOTIF.

Further research directions include: ① The disturbance set can be further reduced by leveraging linearization methods for the nonlinear vehicle system to reduce the conservatism of the SMPAC framework. ② The embedding of state-of-the-art motion planning approaches can be implemented in the SMPAC framework for improved capability.

Declaration of competing interest

The authors declare that they have no known competing financial interests or personal relationships that could have appeared to influence the work reported in this paper.

Acknowledgments

This work was supported by the National Natural Science Foundation of China (51875061) and China Scholarship Council (202206050107).

Appendix A

The Components of Candidate Trajectories:

$$\begin{aligned}
 \mathbf{T}_1 &= \begin{bmatrix} 1 & 0 & 0 & 0 & 0 \\ 0 & 1 & 0 & 0 & 0 \\ 0 & 0 & 2 & 0 & 0 \\ 0 & 1 & 2t_1 & 3t_1^2 & 4t_1^3 \\ 0 & 0 & 2 & 6t_1 & 12t_1^2 \end{bmatrix}, \\
 \mathbf{P}_1 &= \begin{bmatrix} a_1^{(1)} & a_1^{(2)} & \cdots & a_1^{(n_s)} \\ a_2^{(1)} & a_2^{(2)} & \cdots & a_2^{(n_s)} \\ \vdots & \vdots & \ddots & \vdots \\ a_5^{(1)} & a_5^{(2)} & \cdots & a_5^{(n_s)} \end{bmatrix}, \\
 \mathbf{S}_1 &= \begin{bmatrix} s(0) & \dot{s}(0) & \ddot{s}(0) & \dot{s}(t_1)^{(1)} & \ddot{s}(t_1) \\ s(0) & \dot{s}(0) & \ddot{s}(0) & \dot{s}(t_1)^{(2)} & \ddot{s}(t_1) \\ \cdots & \cdots & \cdots & \cdots & \cdots \\ s(0) & \dot{s}(0) & \ddot{s}(0) & \dot{s}(t_1)^{(n_s)} & \ddot{s}(t_1) \end{bmatrix}. \\
 \mathbf{T}_2 &= \begin{bmatrix} 1 & 0 & 0 & 0 & 0 & 0 \\ 0 & 1 & 0 & 0 & 0 & 0 \\ 0 & 0 & 2 & 0 & 0 & 0 \\ 1 & t_1 & t_1^2 & t_1^3 & t_1^4 & t_1^5 \\ 0 & 1 & 2t_1 & 3t_1^2 & 4t_1^3 & 5t_1^4 \\ 0 & 0 & 2 & 6t_1 & 12t_1^2 & 20t_1^3 \end{bmatrix}, \\
 \mathbf{P}_2 &= \begin{bmatrix} b_1^{(1)} & b_1^{(2)} & \cdots & b_1^{(n_d)} \\ b_2^{(1)} & b_2^{(2)} & \cdots & b_2^{(n_d)} \\ \vdots & \vdots & \ddots & \vdots \\ b_6^{(1)} & b_6^{(2)} & \cdots & b_6^{(n_d)} \end{bmatrix}, \\
 \mathbf{S}_2 &= \begin{bmatrix} d(0) & \dot{d}(0) & \ddot{d}(0) & \dot{d}(t_1)^{(1)} & \ddot{d}(t_1) \\ d(0) & \dot{d}(0) & \ddot{d}(0) & \dot{d}(t_1)^{(2)} & \ddot{d}(t_1) \\ \cdots & \cdots & \cdots & \cdots & \cdots \\ d(0) & \dot{d}(0) & \ddot{d}(0) & \dot{d}(t_1)^{(n_d)} & \ddot{d}(t_1) \end{bmatrix}.
 \end{aligned} \tag{A1}$$

$$\begin{aligned}
 \mathbf{T}_2 &= \begin{bmatrix} 1 & 0 & 0 & 0 & 0 & 0 \\ 0 & 1 & 0 & 0 & 0 & 0 \\ 0 & 0 & 2 & 0 & 0 & 0 \\ 1 & t_1 & t_1^2 & t_1^3 & t_1^4 & t_1^5 \\ 0 & 1 & 2t_1 & 3t_1^2 & 4t_1^3 & 5t_1^4 \\ 0 & 0 & 2 & 6t_1 & 12t_1^2 & 20t_1^3 \end{bmatrix}, \\
 \mathbf{P}_2 &= \begin{bmatrix} b_1^{(1)} & b_1^{(2)} & \cdots & b_1^{(n_d)} \\ b_2^{(1)} & b_2^{(2)} & \cdots & b_2^{(n_d)} \\ \vdots & \vdots & \ddots & \vdots \\ b_6^{(1)} & b_6^{(2)} & \cdots & b_6^{(n_d)} \end{bmatrix}, \\
 \mathbf{S}_2 &= \begin{bmatrix} d(0) & \dot{d}(0) & \ddot{d}(0) & \dot{d}(t_1)^{(1)} & \ddot{d}(t_1) \\ d(0) & \dot{d}(0) & \ddot{d}(0) & \dot{d}(t_1)^{(2)} & \ddot{d}(t_1) \\ \cdots & \cdots & \cdots & \cdots & \cdots \\ d(0) & \dot{d}(0) & \ddot{d}(0) & \dot{d}(t_1)^{(n_d)} & \ddot{d}(t_1) \end{bmatrix}.
 \end{aligned} \tag{A2}$$

References

- [1] Yurtsever E, Lambert J, Carballo A, Takeda K. A survey of autonomous driving: common practices and emerging technologies. *IEEE Access* 2020;8:58443–69.
- [2] Wang J, Huang H, Li K, Li J. Towards the unified principles for level 5 autonomous vehicles. *Engineering* 2021;7(9):1313–25.
- [3] Paré PE, Hashemi E, Stern R, Sandberg H, Johansson KH. Networked model for cooperative adaptive cruise control. *IFAC-PapersOnLine* 2019;52(20):151–6.
- [4] Claybrook J, Kildare S. Autonomous vehicles: no driver...no regulation? *Science* 2018;361(6397):36–7.
- [5] Bissell D. Automation interrupted: how autonomous vehicle accidents transform the material politics of automation. *Polit Geogr* 2018;65:57–66.
- [6] Birch J, Rivett R, Habli I, Bradshaw B, Botham J, Higham D, et al. Safety cases and their role in ISO 26262 functional safety assessment. In: Bitsch F, Guiochet J, Kaàniche M, editors. *Computer safety, reliability, and security*; 2020 Sep 16–18; Lisbon, Portugal. Berlin: Springer; 2013. p. 154–65.
- [7] Wang H, Lu B, Li J, Liu T, Xing Y, Lv C, et al. Risk assessment and mitigation in local path planning for autonomous vehicles with LSTM based predictive model. *IEEE Trans Autom Sci Eng* 2022;19(4):2738–49.
- [8] Schmittner C, Griessnig G, Ma Z. Status of the development of ISO/SAE 21434. In: Larrucea X, Santamaria I, O'Connor R, Messnarz R, editors. *Systems, software and services process improvement*; 2018 Sep 5–7. Cham: Springer; 2018. p. 504–13.
- [9] Ziegler J, Werling M, Schroder J. Navigating car-like robots in unstructured environments using an obstacle sensitive cost function. In: *Processings of the 2008 IEEE Intelligent Vehicles Symposium*; 2008 Jun 4–6; Eindhoven, Netherlands. Piscataway: IEEE; 2008. p. 787–91.
- [10] Anderson SJ, Karumanchi SB, Iagnemma K. Constraint-based planning and control for safe, semi-autonomous operation of vehicles. In: *Proceedings of the 2012 IEEE Intelligent Vehicles Symposium*; 2012 Jun 3–7; Madrid, Spain. Piscataway: IEEE; 2012. p. 383–8.
- [11] Kuwata Y, Teo J, Fiore G, Karaman S, Frazzoli E, How JP. Real-time motion planning with applications to autonomous urban driving. *IEEE Trans Control Syst Technol* 2009;17(5):1105–18.
- [12] Werling M, Ziegler J, Kammel S, Thrun S. Optimal trajectory generation for dynamic street scenarios in a Frenét Frame. In: *Proceedings of the 2010 IEEE International Conference on Robotics and Automation*; 2010 May 3–7; Anchorage, AK, USA. Piscataway: IEEE; 2010. p. 987–93.
- [13] Han L, Yoshiro H, Tehrani Nik Nejad H, Do QH, Mita S. Bézier curve based path planning for autonomous vehicle in urban environment. In: *Proceedings of the 2010 IEEE Intelligent Vehicles Symposium*; 2010 Jun 21–24; La Jolla, CA, USA. Piscataway: IEEE; 2010. p. 1036–42.
- [14] Maekawa T, Noda T, Tamura S, Ozaki T, Machida K. Curvature continuous path generation for autonomous vehicle using B-spline curves. *Comput Aided Des* 2010;42(4):350–9.
- [15] Lim W, Lee S, Sunwoo M, Jo K. Hierarchical trajectory planning of an autonomous car based on the integration of a sampling and an optimization method. *IEEE Trans Intell Transp Syst* 2018;19(2):613–26.
- [16] Huang Y, Ding H, Zhang Y, Wang H, Cao D, Xu N, et al. A motion planning and tracking framework for autonomous vehicles based on artificial potential field elaborated resistance network approach. *IEEE Trans Ind Electron* 2020;67(2):1376–86.
- [17] Wu J, Huang Z, Hu Z, Lv C. Toward human-in-the-loop AI: enhancing deep reinforcement learning via real-time human guidance for autonomous driving. *Engineering* 2023;21:75–91.
- [18] Hashemi E, He X, Johansson KH. A Dynamical game approach for integrated stabilization and path tracking for autonomous vehicles. In: *Proceedings of the 2020 American Control Conference (ACC)*; 2020 Jul 1–3; Denver, CO, USA. Piscataway: IEEE; 2020. p. 4108–13.
- [19] Yang K, Tang X, Qin Y, Huang Y, Wang H, Pu H. Comparative study of trajectory robust control for automated vehicles via model predictive control and robust H-infinity state feedback control. *Chin J Mech Eng* 2021;34(1):74.
- [20] Hashemi E, Qin Y, Khajepour A. Slip-aware driver assistance path tracking and stability control. *Control Eng Pract* 2022;118:104958.
- [21] Brunke L, Greeff M, Hall AW, Yuan Z, Zhou S, Panerati J, et al. Safe learning in robotics: from learning-based control to safe reinforcement learning. *Annu Rev Control Robot Auton Syst* 2022;5(1):411–44.
- [22] Wang H, Huang Y, Khajepour A, Zhang Y, Rasekhipour Y, Cao D. Crash mitigation in motion planning for autonomous vehicles. *IEEE Trans Intell Transp Syst* 2019;20(9):3313–23.
- [23] Qin Y, Hashemi E, Khajepour A. Integrated crash avoidance and mitigation algorithm for autonomous vehicles. *IEEE Trans Ind Inform* 2021;17(11):7246–55.
- [24] Collares Pereira G, Wahlberg B, Pettersson H, Mårtensson J. Adaptive reference aware MPC for lateral control of autonomous vehicles. *Control Eng Pract* 2023;132:105403.
- [25] Mayne D. Robust and stochastic model predictive control: are we going in the right direction? *Annu Rev Control* 2016;41:184–92.
- [26] Farina M, Giulioni L, Scattolini R. Stochastic linear model predictive control with chance constraints—a review. *J Process Control* 2016;44:53–67.
- [27] Kerrigan EC, Maciejowski JM. Feedback min-max model predictive control using a single linear program: robust stability and the explicit solution. *Int J Robust Nonlinear Control* 2004;14(4):395–413.
- [28] Mayne DQ, Raković SV, Findeisen R, Allgöwer F. Robust output feedback model predictive control of constrained linear systems. *Automatica* 2006;42(7):1217–22.
- [29] Zheng H, Zheng L, Li Y, Wang K, Zhang Z, Ding M. Varying zonotopic tube RMPC with switching logic for lateral path tracking of autonomous vehicle. *J Franklin Inst* 2022;359(7):2759–87.
- [30] Wischniewski A, Euler M, Gümüs S, Lohmann B. Tube model predictive control for an autonomous race car. *Veh Syst Dyn* 2022;60(9):3151–73.
- [31] Hang P, Xia X, Chen G, Chen X. Active safety control of automated electric vehicles at driving limits: a tube-based MPC approach. *IEEE Trans Transp Electrif* 2022;8(1):1338–49.
- [32] Wu X, Wei C, Tian H, Wang W, Jiang C. Fault-tolerant control for path-following of independently actuated autonomous vehicles using tube-based model predictive control. *IEEE Trans Intell Transp Syst* 2022;23(11):20282–97.
- [33] Feng S, Song Z, Li Z, Zhang Y, Li L. Robust platoon control in mixed traffic flow based on tube model predictive control. *IEEE Trans Intell Transp Syst* 2021;6(4):711–22.
- [34] Althoff M, Rath JJ. Comparison of guaranteed state estimators for linear time-invariant systems. *Automatica* 2021;130:109662.
- [35] Rasekhipour Y, Khajepour A, Chen SK, Litkouhi B. A potential field-based model predictive path-planning controller for autonomous road vehicles. *IEEE Trans Intell Transp Syst* 2017;18(5):1255–67.

- [36] Grüne L. [Analysis and design of unconstrained nonlinear MPC schemes for finite and infinite dimensional systems](#). *SIAM J Control Optim* 2009;48(2):1206–28.
- [37] Althoff M, Grebenyuk D. [Implementation of interval arithmetic in CORA](#) 2016. In: *Proceedings of the 3rd International Workshop on Applied Verification for Continuous and Hybrid Systems*; 2016 Apr 12, Vienna, Austria. Stockport: EasyChair; 2016. p. 91–105.
- [38] Stoican F, Hovd M. [Efficient solution of a qp optimization problem with zonotopic constraints](#). In: *Proceedings of the 2012 IEEE International Conference on Control Applications*; 2012 Oct 3–5; Dubrovnik, Croatia. Piscataway: IEEE; 2013. p. 457–62.
- [39] Liu J, Luo Y, Zhong Z, Li K, Huang H, Xiong H. [A probabilistic architecture of long-term vehicle trajectory prediction for autonomous driving](#). *Engineering* 2022;19:228–39.